
Article:
Alshammari, O.G. orcid.org/0000-0003-3419-8054, Isaac, O.S. orcid.org/0000-0003-3621-5903, Clarke, S.D. orcid.org/0000-0003-0305-0903 et al. (1 more author) (2023) Numerical modelling of blast mitigation of pre-fractal obstacles. International Journal of Protective Structures. ISSN 2041-4196

https://doi.org/10.1177/20414196231192676

Original Research Article

International Journal of
Protective Structures

Numerical modelling of blast mitigation of pre-fractal obstacles

International Journal of Protective Structures
2023, Vol. 0(0) 1–29

DOI: 10.1177/20414196231192676
journals.sagepub.com/home/prs

Omar Ghareeb Alshammari[1,2], Obed Samuelraj Isaac[1,3], Samuel David Clarke[1] and Samuel Edward Rigby[1]

Abstract

The mechanics of downstream blast wave attenuation caused by interaction with obstacles arranged into a pre-fractal shape based on the Sierpinski carpet was numerically investigated using a high-fidelity CFD solver. The blast mitigation was qualitatively and quantitatively assessed for four pre-fractal iterations at three different scaled distances (Z = 1.87, 2.24, 2.99 m/kg$^{1/3}$). Mitigation was seen to occur in zones associated with the location of destructive wave interference patterns in the downstream region. Crucially, these zones were found to widen spatially with increasing pre-fractal iteration, and strong shock-shock interactions that result in load amplification, commonly encountered in downstream regions of a solitary block-like obstacle, were not observed for the more fractal-like obstacles. The mechanisms of attenuation are explored in terms of wave impedance. It is found that pre-fractals reduce wave transmission in the downstream, increase reflection of the blast wave, and enhance trapping within the confines of the pre-fractal obstacle, dramatically changing the directionality and hence the strength of the transmitted wave. Reductions in peak pressure of up to 60% and peak specific impulse of up to 40% were recorded for the highest iteration pre-fractal, that is, obstacles that most closely represent a true fractal, thereby highlighting the effectiveness of such shapes for protective structure design for improved blast mitigation.

Keywords

Numerical modelling, pre-fractal, blast wave interaction, blast mitigation, mechanics

[1]Department of Civil and Structural Engineering, The University of Sheffield, Sheffield, UK
[2]Department of Civil Engineering, College of Engineering, University of Hail, Hail, Saudi Arabia
[3]Thomas Lord Department of Mechanical Engineering and Material Science, Duke University, Durham, NC, USA

Corresponding author:
Omar Ghareeb Alshammari, Department of Civil and Structural Engineering, The University of Sheffield, Mappin Street, Sheffield S1 3JD, UK.
Email: ogalshammari1@sheffield.ac.uk

Introduction

Motivation

Concerns over accidental or terrorist explosions within urban landscapes have risen over the past years, leading to increased research efforts in blast wave attenuation properties of protective barriers. In addition to traditional blast walls, a new type of protective structure has been proposed in recent work which makes use of arrays of limited width barriers such as posts. The interaction of a blast wave with a solid wall of finite width leads to a strong reflection and diffraction around the free edges, allowing the wave to propagate further behind the wall and resulting in complex wave patterns such as the formation of a Mach stem which can result in load amplification (Beyer, 1986). Semi-infinite, nominally rigid obstacles erected around or ahead of a target structure as an array, or a matrix to reflect/deflect the impinging blast, offers the possibility of more completely separating the wavefront, thereby avoiding such magnifying effects downstream. Research on the mitigation potential offered by blast interactions – either by a single or an arrangement of multiple obstacles and various other configurations – have all been summarised in the recent review of Isaac et al. (2022b).

One of the drawbacks of solid protective walls is that they occupy a large area which is not aesthetically desirable, particularly in urban environments. Additionally, the excessive weight of such structures have recently led researchers to consider alternative arrangements, such as optimally spaced obstacles to create a 'fenced wall'. Within the concept of a fence wall, several configurations have been proposed in the literature – fence columns (Hao et al., 2017), steel posts (Xiao et al., 2017, 2020), and a matrix of poles (Chaudhuri et al., 2013; Gautier et al., 2020) – each of which have been shown to substantially alter the downstream blast wave properties. The performance of these 'walls' has been shown to depend on

(i) the geometrical section and shape of individual elements; as they control the development of reflection and diffraction processes (Chaudhuri et al., 2013; Gebbeken and Döge, 2010; Zong et al., 2017), and vortex shedding (Prasanna Kumar et al., 2018; Suzuki et al., 2000).
(ii) the blockage ratio or the porosity ratio; which includes cumulative contributions from the number and size of individual obstacles, number of layers, and horizontal and vertical distances between obstacles in the configuration, all of which can promote a better blast wave attenuation (Chaudhuri et al., 2013; Jin et al. 2019; Skews et al., 1998; Xiao et al. 2017).
(iii) the obstacle pattern within a given matrix (Gautier et al. (2020); (Prasanna Kumar et al, 2018; Niollet et al., 2015).
(iv) the relative position of the barrier between the source of the explosion and the protected structure (Christiansen and Bogosian, 2012; Alshammari et al., 2022).

While these factors have been found to be effective in altering the blast wave properties, it should be noted that they were characterised for single-length-scale scenarios, where the relevant dimensions of an obstacle were similar.

Pre[1]-fractals have certain geometrical characteristics such as scale similarity (Sreenivasan, 1991; Turcotte, 1988), multiple length scales (Higham and Brevis, 2018; Higham et al., 2021; Higham and Vaidheeswaran, 2022), and high surface-to-volume ratio (Werner and Ganguly, 2003) All of these characteristics have been demonstrated to be practical and highly useful for various engineering applications (Dadrasi et al., 2019; Meza et al., 2015; Nguyen-Van et al., 2021). Recently, one such

application, involving shock wave transmission in solids, was studied by Dattelbaum et al. (2020). Using a combination of gas gun impact experiments and numerical modelling, they demonstrated the ability of Sierpinski fractal cubes to absorb shock wave energy. This was possible through refraction/diffraction wave interactions at timescales of the same order of magnitude as the shockwave propagation.

Multi-scale obstacles have also been shown to demonstrate excellent blast mitigation behaviour. Gebbeken et al. (2017) investigated the blast mitigation abilities of hedges and plants, which are, essentially, subsets of pre-fractal shapes that can be found in abundance in the natural world. To further explore the reasons behind the attenuation obtained using these pre-fractal shapes from nature, a more tractable model was employed by Isaac et al. (2022a). In that work, a number of simple pre-fractal objects were investigated for their blast mitigating capabilities, and some promising results were observed. However, the true extent of the mitigation behaviour of multi-scale obstacles is yet to be fully characterised, and therefore their use for protective purpose is currently limited.

Overview

In the aforementioned experimental work of Isaac et al. (2022a), the first three iterations of a Sierpinski carpet pre-fractal were tested, with each obstacle in the set (Figure 1) an iteration of the previous one. It can be seen that, by design, these obstacles automatically incorporate multiple length scales.

The first fractal iteration (pFI-1, Figure 2(a)) contains only a 180 mm square hollow section. The second fractal iteration (pFI-2) has eight additional 60 mm square poles surrounding the 180 mm section, with a 60 mm gap between the 180 mm and 60 mm obstacles (see Figure 2(b)). The third fractal iteration (pFI-3, Figure 2(c)) comprises eight 20 mm square rods surrounding each 60 mm square pipe from the second iteration, with a 20 mm air gap. The fractal dimension for this obstacle is given by $D = \log(N)/\log(S) = 1.89$, where N is the number of copies of the original in each iteration ($N = 8$), and S is the scale factor between an original and its copy ($S = 3$). The height of each of these obstacles is 1 m.

The pre-fractal obstacles were exposed to a 250 g PE4 surface blast loading at 3 different stand-off distances (SoD) of 125 cm, 150 cm, and 200 cm, each measured from the centre of the explosive to the front face of the central obstacle. A triplicate of free-field experiments (pFI-0, a no-obstacle case) was also carried out for all of these SoDs. For these experiments, Hopkinson Cranz

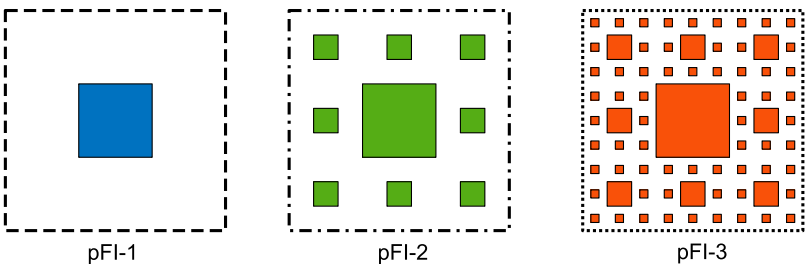

Figure 1. Plan view illustration displaying the first three iterations of a Sierpinski carpet. These designs were also the obstacles chosen for this work – iteration 1 (pFI-1), iteration2 (pF-2), and iteration 3 (pFI-3), as adapted from Isaac et al. (2022a).

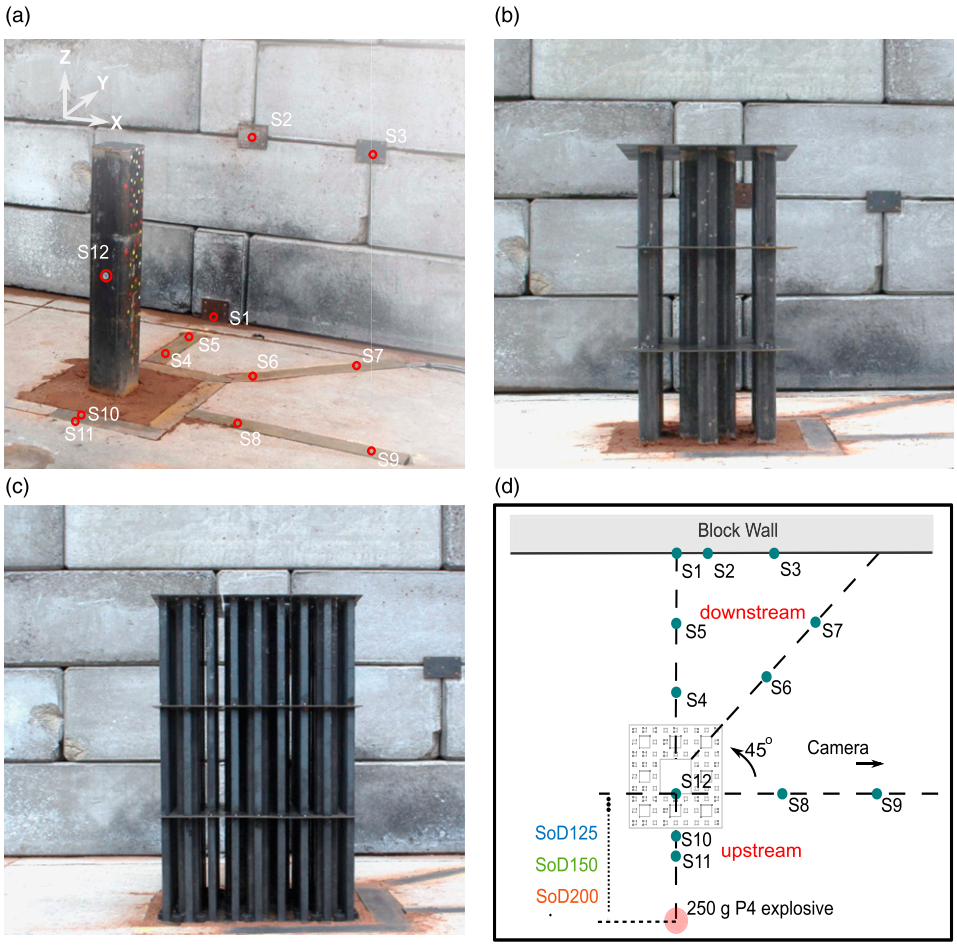

Figure 2. A photograph of each of the pre-fractal shapes (a) pFI-1, (b) pFI-2, and (c) pFI-3, as installed at site. (d) A schematic layout showing the locations of the explosive, the obstacle, the target wall, the camera and the pressure sensors. Figures adapted from Isaac et al. (2022a).

(TNT equivalent) scaled distances were Z_{SOD125} = 1.87 m/kg$^{1/3}$, Z_{SOD150} = 2.24 m/kg$^{1/3}$, and Z_{SOD200} = 2.99 m/kg$^{1/3}$, assuming a PE4 TNT equivalence of 1.20 (Rigby and Sielicki, 2015).

The blast wave interaction process was quantitatively and qualitatively investigated using pressure measurements and a high speed camera. A total of 12 pressure sensors were placed at locations both along the upstream, and the downstream regions (see Figure 2(d)) of the obstacle. The resulting incident and reflected overpressure histories were used to carefully extract the peak pressure, peak specific impulse and arrival time. To visualise the evolution of shock patterns, a high speed camera was used to capture time-resolved images against a zebra-board background.

The important observations from the experiments were as follows:

- The reflected pressure measurements on the block wall showed that: (i) pressure mitigation became significant with increasing complexity of the obstacles and this attenuation was quantitatively similar within the range of blast intensities (SoDs) that were tested. However,

the attenuation pattern of specific impulse did not correlate well with the complexity of a given pre-fractal configuration and it was also found to be sensitive to the SoD. (ii) The delay in the arrival time was found to be a function of the pre-fractal iteration number.

- The incident pressure gauges downstream and within the vicinity of the obstacle showed that: (i) pressure and impulse mitigations were only pronounced for shapes that more closely resembled a true fractal, that is, pFI-3. Conversely, for the simpler obstacles (pFI-1 & pFI-2) a pressure *enhancement* was observed. This was proposed to be due to the pressure waves coalescing and re-forming after being deflected around the obstacle, but this has not been confirmed through direct observation. This enhancement was only for a limited distance downstream and did not persist. (ii) For such pre-fractal configurations, regions beyond 6 primary length scales (6×180 mm) along the 45° line downstream (at sensor 7 in Figure 2(d)) were found to be undisturbed by the obstacle, indicating that the effectiveness of mitigation is spatially limited.
- It was also reported that when an obstacle becomes more fractal-like (such as pFI-3), a consistent mitigation pattern of peak pressure and specific impulse was observed. This was attributed to 'wave trapping' within this obstacle and an enhanced break-up of the incident blast wavefront which effectively prevented it from coalescing behind the obstacle. This was also verified using the high speed video footage, but again has not been confirmed through direct observation.

While it is clear that an enhanced blast mitigation occurs when the configuration shape approaches a fractal-like shape such as iteration 3, the following questions naturally arise.

1. What are the precise mechanisms governing this mitigation?
2. What amount of additional mitigation would be present if the complexity of pre-fractal is increased further (i.e. the 4th iteration)?
3. What is the required fidelity of numerical simulations in order to faithfully replicate this behaviour?
4. What is the relationship between the spatial bounds of the mitigation and the fractal iteration and size?

This paper thus aims to address the above and it is organised in the following manner. An overview of numerical modelling using Apollo Blastsimulator is first presented followed by a mesh sensitivity analysis for obstacle-wave interaction phenomena. Then, CFD numerical models are extensively validated against the experimental measurements. Using this validated model, a comprehensive numerical study on the effectiveness of blast mitigation of pre-fractal obstacles is performed in an attempt to fully characterise the mechanics of interaction.

Numerical methodology

Modelling in APOLLO blastsimulator

Overview. Apollo Blastsimulator software (hereafter referred to as Apollo) is a specialised computational fluid dynamics (CFD) tool that was developed by Fraunhofer EMI (2018) for simulating explosions, and the gas dynamics of blast wave propagation. This solver has been extensively used to solve blast propagation and blast-obstacle interaction problems (Alshammari et al., 2022; Dennis et al., 2021; Farrimond et al., 2023; Whittaker et al., 2019; Pannell et al., 2019, 2021).

The computational domain in Apollo is based on a Cartesian grid system defined in terms of the zone length, L, at the coarser level, and the cell length, h, (called resolution) at the finer level. The

ultimate resolution is automatically computed in Apollo as $h = L/2^N$ on specifying the zone length L and a resolution level N ranging from 0 to 9. This solver can carry out dynamic mesh adaptation (DMA), map the flow solution from 1D to 3D and also between 3D stages.

Explosives in this work were modelled as C4, which is nominally identical to PE4 (Bogosian et al., 2016). The Chapman-Jouget model was used in Apollo to model detonation and the Jones-Wilkins-Lee (JWL) equation of state was used to model the products of reaction.

Model setup and domain size. The numerical modelling in this study replicates the geometry of the experimental work in Isaac et al. (2022a), in which 0.25 kg hemispheres of PE4 were detonated on a flat ground surface at different stand-off distances from the central obstacle. Figure 3 shows the

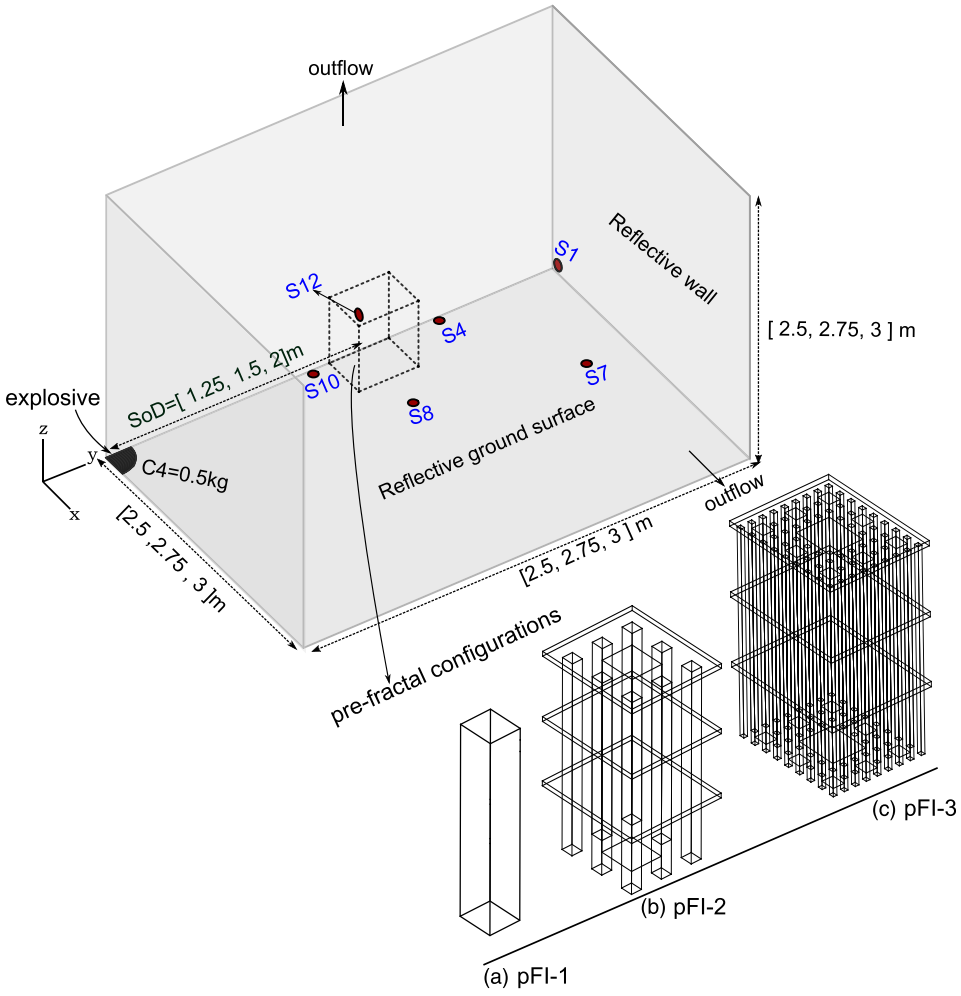

Figure 3. The 3D symmetric numerical domain octant for 12 different numerical configurations involving a combination of SoDs (viz., 1.25, 1.50, 2.00 m) and pre-fractal configurations – (a) pFI-1, (b) pFI-2, (c) pFI-3. The no obstacle configuration pFI-0 has not been specifically marked out as it pertains to the free-field scenario.

general numerical model layout adopted for each of the 12 simulations (3 SoDs and 4 pre-fractal arrangements, including pFI-0, i.e. free-field). Octant domains used for the 3D simulations had different dimensions based on the stand-off distance between the explosive and the obstacle, namely 2.5 × 2.5 × 2.5 m, 2.75 × 2.75 × 2.75 m, and 3 × 3 × 3 m for the 1.25 m, 1.50 m, and 2.0 m SoDs, respectively. Rigid boundaries were located along the x = 0, y = 0, and z = 0 planes, with a reflecting wall at either y = 2.5, 2.75, and 3 m for each different SoD. Outflow planes were specified for the remaining two sides. Results at 6 sensors of the 12 sensor locations are explored in detail in this article, namely: S_1, S_7, S_4, S_8, S_{10}, and S_{12}. Sensor locations for each series of models with a common SoD are listed in Table 1.

Mesh sensitivity analysis

Mesh convergence analysis was carried out in two stages:

Stage 1: An analysis of the effect of the ultimate cell length, $h = L/2^N$ on blast loading parameters with respect to the stand-off distance was carried out for the free-field scenario. This was used to derive the optimal cell length for a variety of blast intensities.

Stage 2: Once the required free-field resolution was determined, further investigations were performed on the sensitivity of the solution to the ratio of the cell length to the smallest length scale of the pre-fractal elements.

Free-field scenario. A series of numerical simulations using different cell sizes was carried out for the free-field case (pFI-0) at the closest SoD (1.25 m) as seen in Figure 3.[2] The explosive was placed at a total stand-off distance of 2.5 m from the rigid wall to match the geometry of the experimental work of Isaac et al. (2022a). Pressure data from the five sensors in the corresponding experimental configuration (pFI-0-SoD125), were used for comparison against CFD data. Of these, four were incident sensors (S_4, S_7, S_8, and S_{10}) and one was a reflective sensor (S_1), resulting in 5 different Hopkinson scaled distances: Z_{S1} = 3.97 m/kg$^{1/3}$, Z_{S4} = 2.86 m/kg$^{1/3}$, Z_{S7} = 3.68 m/kg$^{1/3}$, Z_{S8} = 2.22 m/kg$^{1/3}$, and Z_{S10} = 1.62 m/kg$^{1/3}$ (see Figure 2(d)). As part of a preliminary analysis, 20 sample simulations were run and the results compared against the experimental data from a single sensor (S_1) to iterate towards the optimal cell count to ensure a satisfactory solution. The relevant cell size details including zone length L, resolution level N, and resolution h, for Z_{S1}= 3.97 m/kg$^{1/3}$ have been

Table 1. Sensor coordinates in the numerical model in Figure 3, arranged in terms of distance from the wall for each SoD.

	SoD125				SoD150				SoD200			
	Coordinates (m)				Coordinates (m)				Coordinates (m)			
Sensor number	X	Y	Z	Z [m/kg$^{1/3}$]	X	Y	Z	Z [m/kg$^{1/3}$]	X	Y	Z	Z [m/kg$^{1/3}$]
S_1	0	2.5	0.02	3.97	0	2.75	0.02	4.37	0	3	0.02	4.76
S_7	0.83	2.17	0	3.69	0.83	2.42	0	4.06	0.83	2.67	0	4.44
S_4	0	1.80	0	2.86	0	2.05	0	3.25	0	2.3	0	3.65
S_{12}	0	1.25	0.51	2.14	0	1.50	0.51	2.52	0	2.0	0.51	3.28
S_8	0.64	1.25	0	2.23	0.64	1.50	0	2.59	0.64	2.00	0	3.33
S_{10}	0	1.02	0	1.62	0	1.27	0	2.02	0	1.52	0	2.41

listed in Table 2, and the corresponding cell counts between the charge centre and the sensor S_1 for each of these parameters have been listed in Table 3.

The results of these free-field mesh sensitivity analyses in terms of peak overpressure, peak specific impulse, and the computational time (named 'wall time', short for wall-clock time), have been plotted in Figure 4 against the ultimate cell length (h) normalised against the stand-off distance from S_1. The solid black line represents the average experimental value and the dashed line indicates a 10% deviation from the average experimental value, which has been taken to be an acceptable deviation from the measured value for the purpose of this work.

From these plots, it can be seen that the accuracy of the peak overpressure values depend significantly both on the number of zones and the number of cells between the charge and the target. From these results in Figure 4, a mesh having 'number of zones' 20 and a resolution $h < SoD/160$ can be appropriate for the 10% peak pressure convergence, whilst for the specific impulse, since the zone number is less relevant, the mesh resolution can be relaxed to $h < SoD/30$. Based on this, the cell size has been taken to be 15.62 mm (= SoD/160) for simulating all the free-field cases in Figure 3.

With pre-fractal interaction. While blast loading simulations for a free-field configuration reached convergence with cell element size equal to SoD/160, it is also necessary to refine this value when additional interactions such as wave diffraction/refraction, trapping (Isaac et al. (2022b); Skews et al., 1998), and downstream wave interference (Alshammari et al., 2022; Hahn et al., 2021) are

Table 2. Ultimate cell length in CFD domain for 20 simulations.

	Zone length, L (mm)				
	1250	500	125	100	20
Resolution level	Ultimate cell length, h (mm)				
0	1250	500	125	100	20
1	625	250	62.5	50	10
2	312.5	125	31.25	25	
3	156.25	62.5	15.625	12.5	
4	78.125	31.25			

Table 3. Number of cells between the charge centre and the sensor S_1 for the simulations in Table 2.

	Zone length, L (mm)				
	1250	500	125	100	20
Resolution level	Number of cell elements				
0	2	5	20	25	125
1	4	10	40	50	250
2	8	20	80	100	500
3	16	40	160	200	
4	32	80			

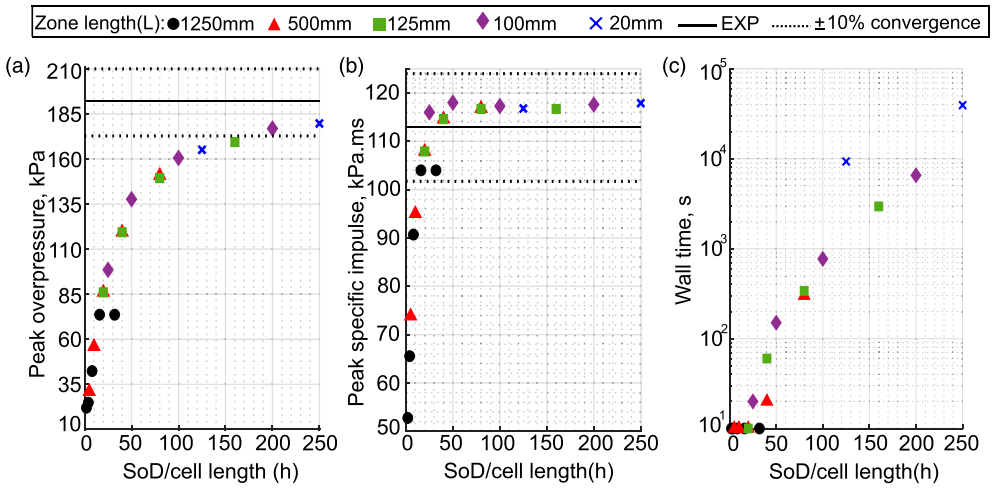

Figure 4. Mesh sensitivity analysis based on data from a single sensor (S_1). The results have been grouped in terms of (a) peak overpressure values, (b) peak specific impulse values, and (c) computational time.

expected to occur. To this end, introducing a new factor, called obstacle-cell ratio, can be useful to determine the optimal mesh element size for simulating the flow around each pre-fractal obstacle. Defined as the width of the obstacle over the mesh element size, this ratio physically represents the number of cells used to discretize the smallest geometry in the obstacle.

The pFI-3 pre-fractal configuration with an SoD of 1.25 m (SoD125) was chosen to replicate the experimental configuration in Figure 2(c) since this obstacle configuration results in particularly complex shock wave interaction patterns, and so the resulting mesh validation would also be applicable to the other configurations, viz., pFI-2 and pFI-1. For this analysis, instead of using a single sensor, all the 6 sensors in Figure 3 have been used to clarify the influence of the obstacle-cell ratio significance on different phenomena: sensor 10 for reflection; sensor 12 for the trapping mechanism at the obstacle location; sensor 8 for the blast directionality changes; sensors 4 and 7 for the incident wave interference in the downstream region; sensor 1 for the reflected wave interference. The location coordinates of these sensors for SoD125 have been given in Table 1 and the computational domain parameters have been listed in Table 4. Here it should be noted that 10 mm cells have been used as the starting size as that would be the smallest size of the obstacle for a half symmetry model (half the size of the 20 mm square rod in pFI-3), and it has been progressively reduced to 2.5 mm. It is worth noting that refining the mesh will dramatically increase the computational effort; the wall-time for the runs using cell elements of 10 mm, 5 mm, and 2.5 mm, were 0.5, 7, and 72 h, respectively.

The resulting peak overpressure and peak specific impulse values have been compared against the corresponding mean experimental values in Figure 5 as both scatter plots and bar charts. The values at downstream sensors (S_4, S_7, and S_1) closely match with the mean experimental values, with slight differences in overpressure occurring with increasing obstacle-cell ratio. The incident sensor S_8 exhibits a fairly good agreement with experimental overpressure data although it underestimates the specific impulse, perhaps due to the simplifications in the ground-surface explosive modelling incorporated in the CFD model. The peak numerical overpressure values in the upstream sensor S_{10} increase as the obstacle-cell ratio increases, with relative error greater than 10%. The numerical specific impulse, however, has successfully converged and falls within the limit of the experimental values. Generally, the values in Figure 5(d) indicate the convergence of peak specific

Table 4. Ultimate cell lengths h for mesh refinement studies of the CFD model in Figure 3(c). NB.: Smallest obstacle width for the symmetric half of pFI-3 is 10 mm.

Zone length = 160 mm	
Cell element length (mm)	Obstacle-cell ratio
10	1
5	2
2.5	4

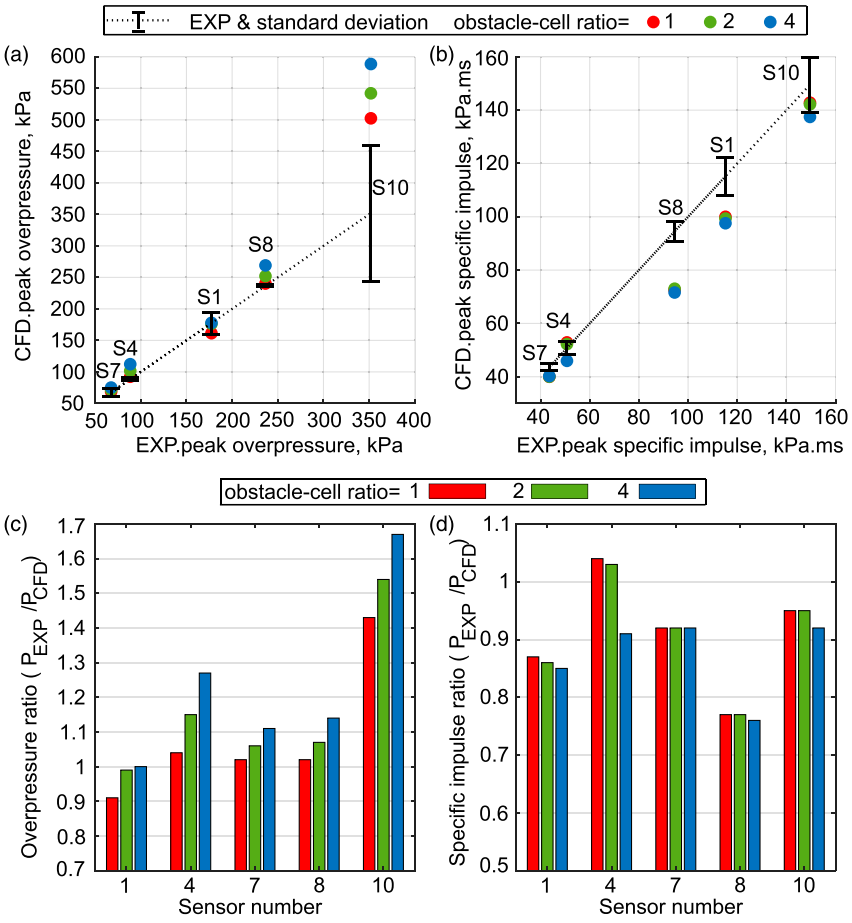

Figure 5. The results of mesh convergence study for pFI-3 at SoD of 1250 mm reported at sensor locations S_1, S_4, S_7, S_8, and S_{10}. (a) & (b) is a scatter plot of the numerical and experimental peak overpressure and peak specific impulse values, respectively. (c) & (d) is a bar graph of the ratios of peak pressure and peak specific impulse, respectively.

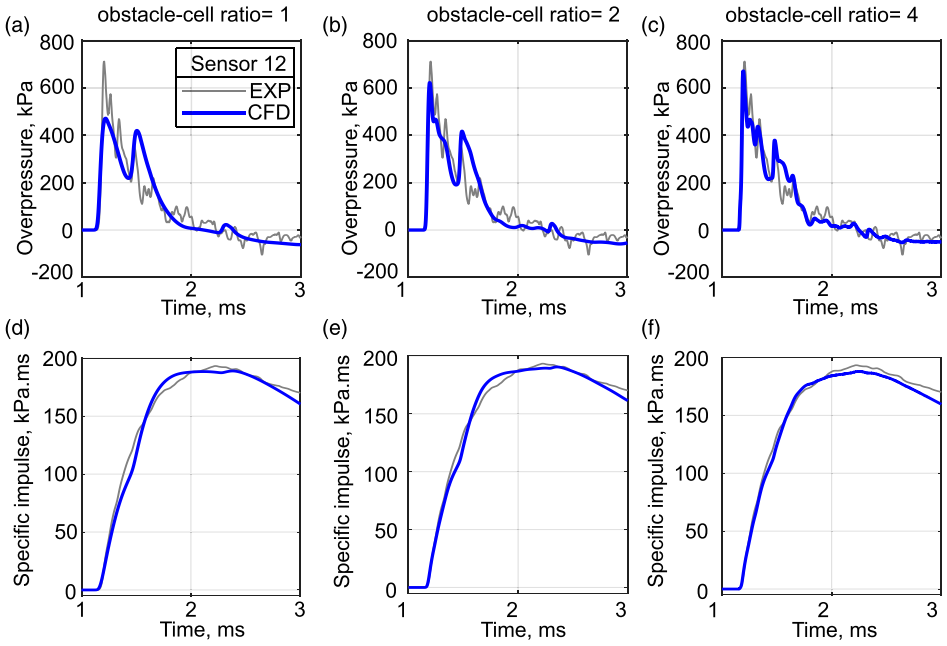

Figure 6. The overpressure (a–c) and specific impulse histories (d–f) at S_{12} for different obstacle-cell ratios.

impulse values for all the chosen mesh sizes. It is also seen (from Figure 5(c) and (d)) that the specific impulse converges faster than the overpressure, which agrees well with the previously reported results for Apollo Blastsimulator (Klomfass, 2018).

Although the influence of obstacle-cell ratio did not play out clearly in Figure 5, a closer look at the overpressure histories (Figure 6(a)–(c)) on the central sensor S_{12}, where the shock trapping occurs, shows the importance of mesh refinement. Obstacle-cell ratios of 2 and 4 could successfully capture the multiple reflections trapped within the obstacle. The specific impulse histories, though, are not greatly influenced by the changes to the number of cells ahead of the smallest pre-fractal element. It is worth remarking that the fourth pre-fractal iteration (pFI-4) will eventually be simulated, and therefore a larger obstacle-cell ratio may be required to achieve convergence.

Numerical model validation

Pressure data validation – free-field configuration. Figure 7 compares numerical and experimental peak overpressure and specific impulse for the 1.25 m stand-off, iteration 0 (free-field) tests using the converged mesh size of h = 15.62 mm (satisfying the SoD/160 criterion outlined previously). As a reminder, S_4, S_7, S_8, and S_{10} are incident gauges and S_1 reflective. The numerically generated peak overpressure and peak specific impulse clearly match the experimental data consistently across a range of scaled distances. This shows that the Apollo software can faithfully recreate mid-field blast loading for the previously outlined mesh sizes.

Next, validation of blast wave interaction with the iteration 3 pre-fractal obstacle pFI-3 is presented (see Figure 3(c)) using the previously outlined mesh size of 2.5 mm, for which the obstacle-cell size ratio was 4. The numerical overpressure and specific impulse histories of the downstream sensors (S_1, S_4), the central pole sensor (S_{12}), and the upstream sensor (S_{10}) have been

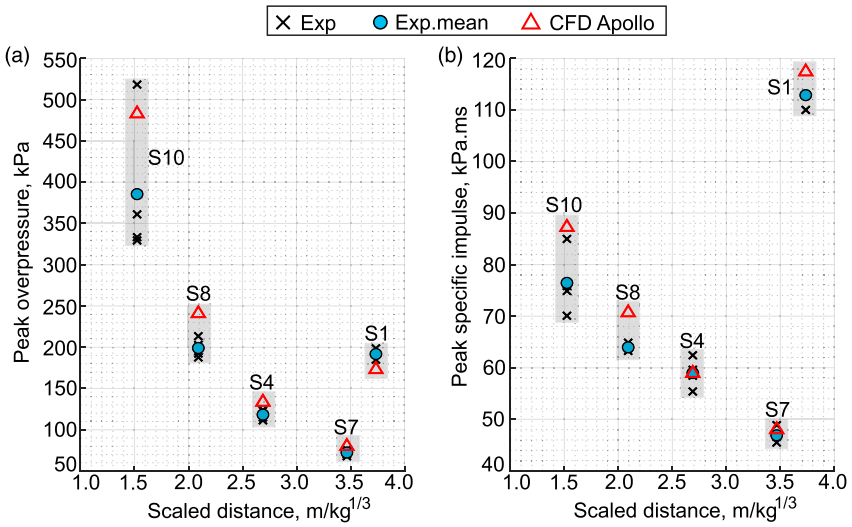

Figure 7. The validation of free-field scenario of all sensors in terms of: (a) peak overpressure and (b) peak specific impulse.

compared for each SoD. In addition, a qualitative comparison was made between a high-speed camera image and the numerically generated image of the shock front disturbance. The total run time of these additional two simulations for the SoD150 and SoD200 was 144 h.

Pressure data validation – blast interaction with a pre-fractal

A time history comparison for numerical and experimental measurements in the downstream region are shown for S_1 and S_4 in Figures 8 and 9, respectively. The reflective blast loading measurements for S_1 match excellently with experimental patterns for different blast wave intensities. Similarly, the incident pressure and impulse values at S_4 show a fairly good overlap. The increasing mismatch in peak overpressure values with SoD (see Figure 9(c)) could be due to simplifications in the modelling ground-surface explosive interaction in the near-field region.

Figure 10 shows an overlay plot of numerical and experimental data for S_{12}, which is mounted centrally on the front face of the 180 mm obstacle in the pFI-3 configuration. These plots are for the overpressure and specific impulse histories at all stand-off distances considered in this work, viz., 1.25 m^3, 1.50 m, and 2.00 m. Again, it can be seen that the software has captured the complex overpressure histories with multiple peaks which arise due to wave trapping quite well. The specific impulse history has also been captured well, implying that the use of obstacle/cell ratio of 4 for blast interaction for a potential fourth iteration of similar pre-fractals is quite appropriate.

Additionally, a sensor in the upstream region (S_{10}) was also chosen to validate the CFD data. The experimental overpressure values for this location (in Figure 11(a)–(c)) consist of multiple peaks; the first from the incident wave and the remainder from reflections off the obstacle. While the behaviour of the numerical model is excellent in predicting these reflected waves, the peak incident overpressure in Figure 11(b) and (c) has been overestimated due to mesh size related constraints as explained earlier (Figure 5(a)). The important features of the specific impulse history though, have been captured successfully by Apollo (in Figure 11(d)–(f)), proving its ability to recreate these experiments.

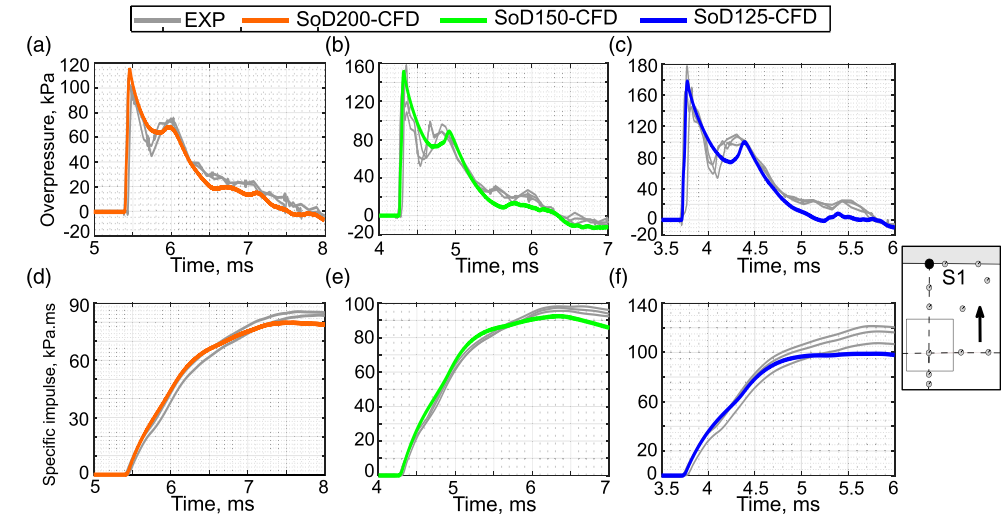

Figure 8. The numerical and experimental measurements for pFI-3 compared at S_1. Overpressure histories for (a to c) SoD = 2 m, 1.5 m, 1.25 m, respectively. Specific impulse histories for (d to f) SoD = 2 m, 1.5 m, and 1.25 m, respectively.

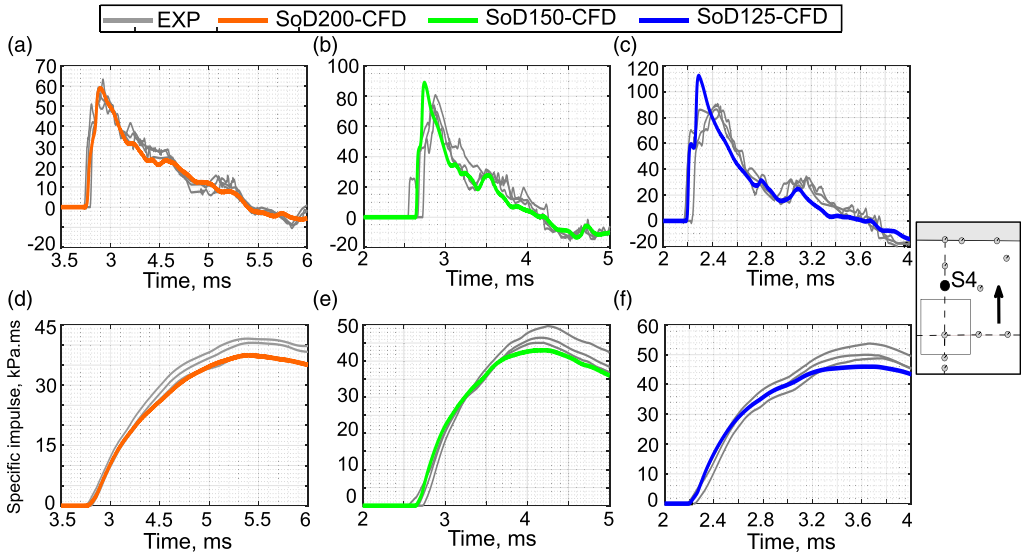

Figure 9. The numerical and experimental measurements for pFI-3 compared at S_4. Overpressure histories for (a to c) SoD = 2 m, 1.5 m, 1.25 m, respectively. Specific impulse histories for (d to f) SoD = 2 m, 1.5 m, and 1.25 m, respectively.

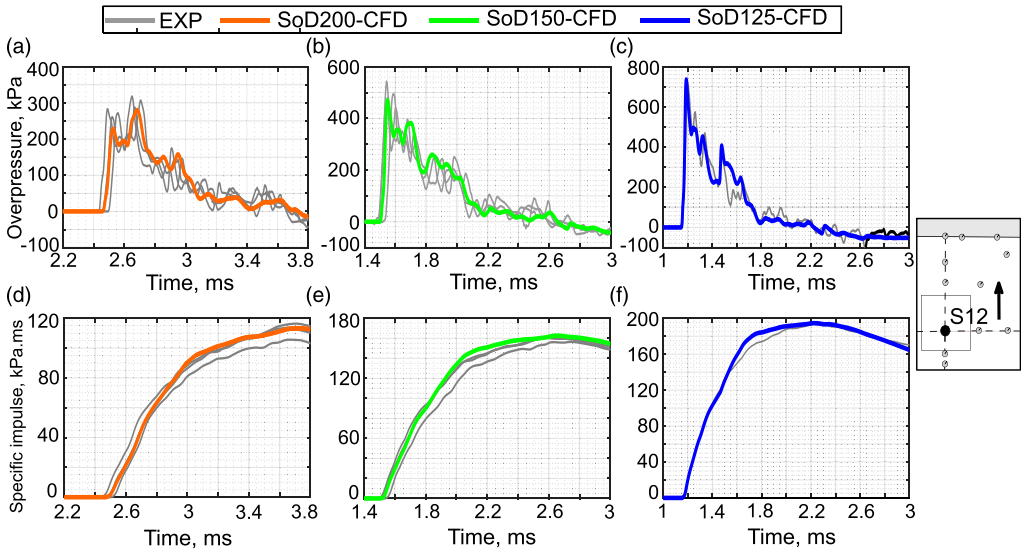

Figure 10. The numerical and experimental measurements at S_{12} for pFI-3. The overpressure histories are compared for SoD = (a) 2 m, (b) 1.5 m, and (c) 1.25 m. The respective specific impulse history comparisons for SoDs = (d) 2 m, (e) 1.5 m, and (f) 1.25 m.

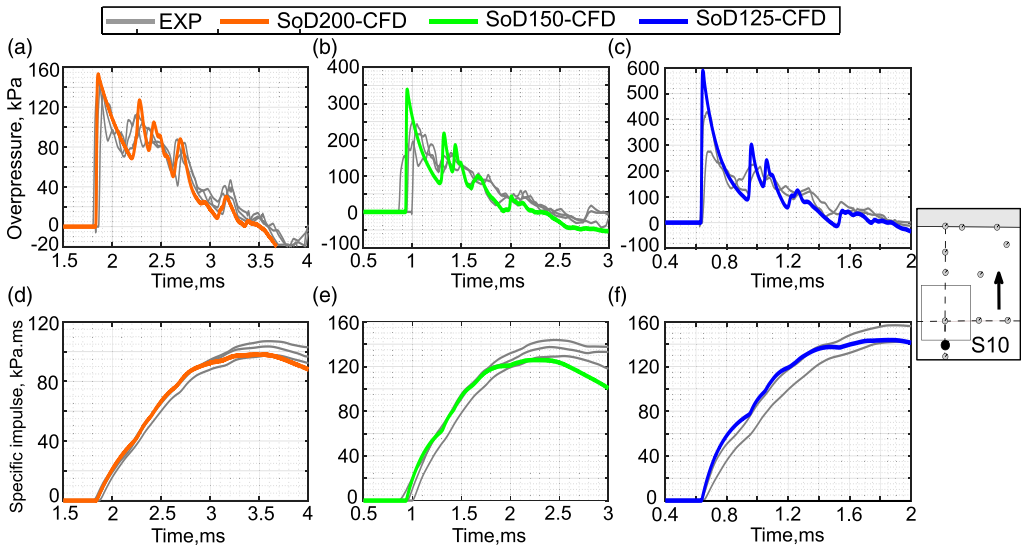

Figure 11. The numerical and experimental measurements at S_{10} for pFI-3. The overpressure histories are compared for SoD = (a–c) 2 m, 1.5 m, and 1.25 m. The respective specific impulse history comparisons for SoDs = (d–f) SoD = 2 m, 1.5 m, and 1.25 m.

Shock shape validation – high speed camera images. Apart from these spatially localised validations, an overall snapshot of the flow field was also used to qualitatively compare against the photographs of the shock wave captured experimentally. In the experimental work, using a high speed camera, distortions while imaging a zebra pattern – due to the presence of a shock wave in its foreground – were captured. Artificial schlieren images were derived from the CFD data (using Paraview) at different time instants as shown in Figure 12. These comparative images show that Apollo has fairly successfully captured the reflections of the incident shock wave at t = 3 ms (Figure 12(a) and (b)), acknowledging the non-exact nature of the overlays of the experimental video stills. Even the transmission of waves through the obstacles (green lines In Figure 12(c) and (d)) demonstrating the breakup of the shock front that leads to significant mitigation, has been captured reasonably well. This qualitative agreement is not surprising giving the level of quantitative agreement seen previously.

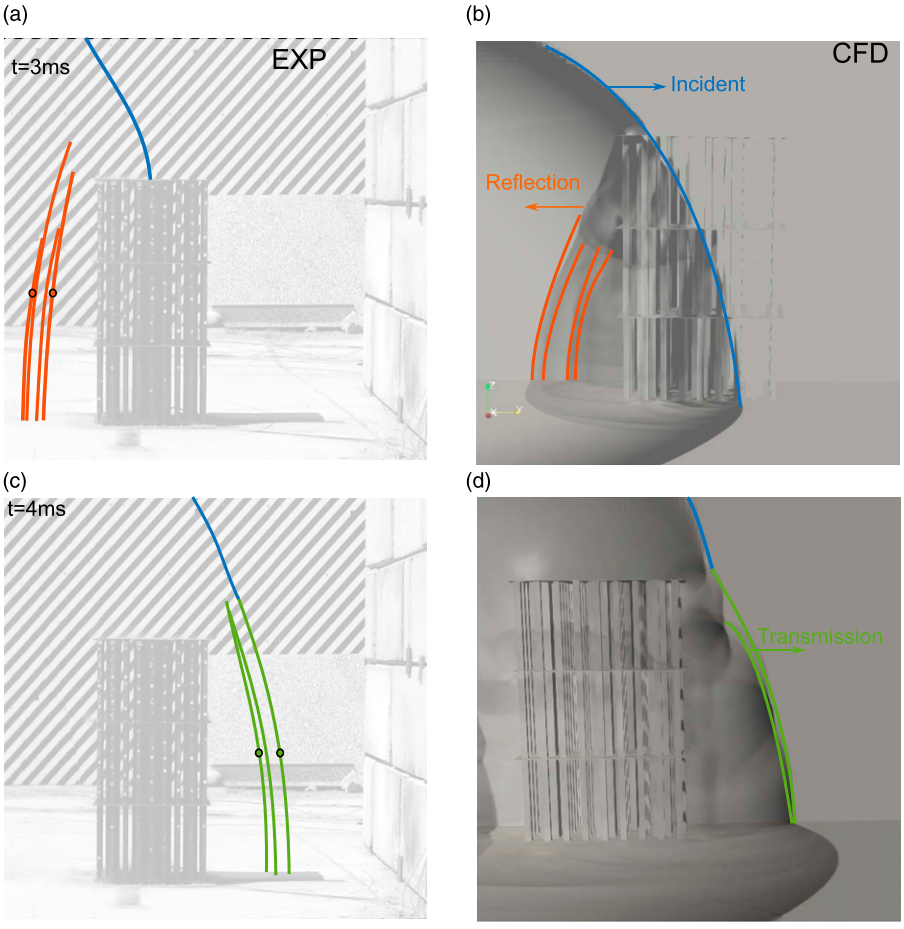

Figure 12. Qualitative comparison of shock fronts at two different time instants between experiments (L) and numerical data (R) for pFI-3-SoD200. Experimental photographs have been adapted from Isaac et al. 2022a. The comparisons have been made at (a),(b) 3 ms and (c),(d) 4 ms after detonation. The incident wave (blue); reflected wave (red); and transmitted (green) wave in these images are seen to corroborate fairly well.

In the light of these extensive validation runs, it can be stated that Apollo can reliably predict the blast loading for all wave interferences occurring downstream of similar obstacles.

Simulation details

Simulations with a wall. After Apollo CFD was verified for its ability to simulate blast wave interaction with complex pre-fractal iterations such as pFI-3 in the previous section, a new set of simulations were performed to address the main research questions using the previously identified mesh size requirements. These new simulations were run for the pFI-1 and pFI-2 configurations used in the experimental set-up (see Figure 3(a) and (b)) to qualitatively study the mechanism of the experimentally observed mitigation. The results from the previous simulations were retained and re-used for pFI-3. In addition to these, a configuration that is the fourth iteration of the Sierpinski carpet based fractal (the virtual pFI-4, illustrated in Figure 13) was created. This obstacle has 5 mm square rods surrounding each 20 mm square pipe from the pFI-3 configuration, with a 7.5 mm air gap[4]. These simulations were then used to numerically compute the mitigation enhancement on increasing pre-fractal complexity (i.e. iteration number). The enhancement was rationalised in terms of wave impedance, represented in general by the difference in the measured value ahead of, and behind the obstacle at fixed locations.[5] These locations sensor_{in} & sensor_{out}, which were retained for all the obstacles, are shown for pFI-4 in Figure 13. Table 5 summarises this list of simulations with a rigid wall 1.25 m behind the central obstacle, with the aim of answering the first two research questions in this study (see *Introduction*).

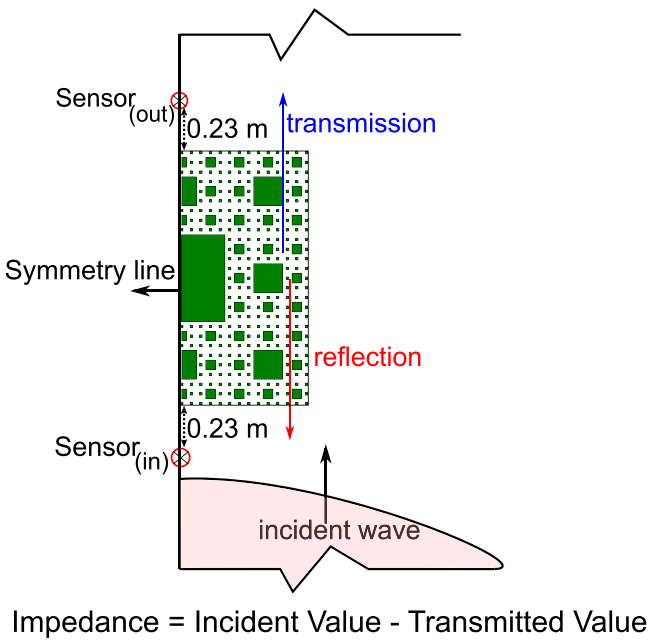

Figure 13. Input parameters for the impedance measurement of an incident blast wave. This is illustrated here for the pFI-4 configuration.

Table 5. Details of the additional simulations including a wall for a domain size as in Figure 3.

No.	Pre-fractal configuration in Figure 3	Stand-off distance (SoD) (m)	Explosive charge	Domain dimensions [X, Y, Z] in m	Element size (mm)	Simulation time
1	pFI-1	1.25	0.25 kg C4	2.50 × 2.50 × 2.50	2.5	70 h
2	pFI-2					
3	pFI-3					
4	pFI-4					
5	pFI-1	1.50		2.75 × 2.75 × 2.75		72 h
6	pFI-2					
7	pFI-3					
8	pFI-4					
9	pFI-1	2.00		3.0× 3.0 × 3.0		75 h
10	pFI-2					
11	pFI-3					
12	pFI-4					

Simulations without a wall. The relationship between pre-fractal iteration number and the pre-fractal's zone of influence (spatial bounds of mitigation) was subsequently investigated by developing a new set of numerical models (Figure 14). This aims to address the final research question posed in this study (see *Introduction*). In these new simulations, the rigid wall in Figure 3 was removed in order to eliminate complications to the downstream flow field that arise due to reflection. A 3D quarter symmetric CFD domain, with dimensions of 2.8 m× 4.4 m × 2.8 m was chosen to simulate each of the 4 pre-fractal obstacles facing a blast load from the detonation of a hemispherical 0.25 kg C4 (modelled as 0.5 kg sphere in Apollo). The stand-off distance between the explosive centre and the front face of the central obstacle within the pre-fractal was 1.25 m and the other distances were not simulated. This is because SoD125 gives a single Hopkinson Cranz scaled distance of 1.87 m/kg$^{1/3}$, which is sufficiently representative of changes in the mitigation behaviour for all these scaled distances (Alshammari et al., 2022). Therefore, 5 simulations were carried out, one for each pre-fractal arrangement, and one for the reference (free-field) scenario, to calculate the mitigation.

The domain of observation was extended to 10D on either side of the obstacle, where D is the widest length scale in any obstacle (180 mm). A uniform array of sensors (numbering a total of 1296) was placed on the ground, downstream of the obstacle to quantify the mitigation in terms of ratios of overpressure and specific impulse (Equation (1)). The height of the obstacles in the 3D model was 1 m.

$$P_{ratio} = P_{max,\,obstructed} / P_{free} \tag{1a}$$

$$I_{ratio} = I_{max,\,obstructed} / I_{free} \tag{1b}$$

Results and discussion

Understanding the mechanics of mitigation

The mechanics of fractal-like blast loading mitigation are explored using fringe plots for the first three obstacle iterations. Figure 15 shows a comparison of the wave propagation behaviour at

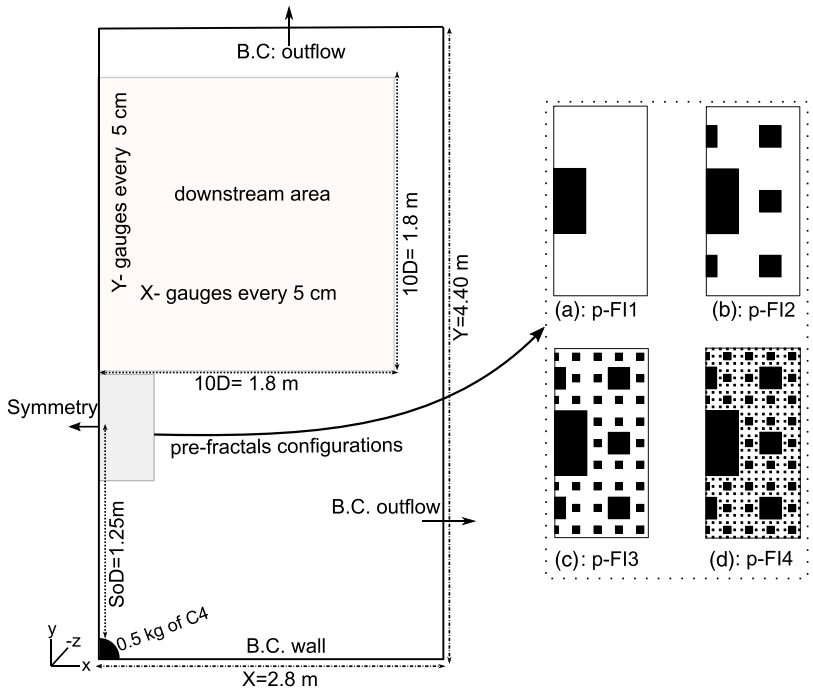

Figure 14. A schematic diagram of the plan view of the 3D numerical model, with the inset showing the obstacles: (a) pFI-1 (b) pFI-2 (c) pFI-3 and the virtual obstacle (d) pFI-4.

different times for the SoD200 simulations (numbers 9, 10, and 11 in Table 5). The initial observation is that the strength of the reflected wave for the most fractal-like shape (pFI-3, see right of Figure 15(b)) is much larger than the reflected wave from the previous iterations. Moreover, the blast wave trapping is considerably more intense in pFI-3 at 2.8 ms (Figure 15(b)) due to its high area-volume ratio and large number of reflecting surfaces (air gap is only 20 mm). This trapping is not very evident for the pFI-2 arrangement since the 60 mm air gap results in reduced blockage. The pFI-1, on the other hand, experiences only a normal reflection at the front face and a diffraction off its corners, resulting in only a minimal mitigation. As a result, the proportion of the pressure wave transmitted through these obstacles is clearly weaker at t = 4 ms for pFI-3 arrangement (right end of Figure 15(c)). To reiterate, this is due to the strong break-up of the wave front for pFI-3 as compared to pFI-2 and pFI-1 (Figure 15(c)).

The changes to the directionality of the incident wave, and the formation of vortices were then visualised using streamline plots for all the obstacles, (at 4 ms after detonation). Streamline plots in terms of the velocity ($\overrightarrow{v}$) component parallel to the direction of flow (y-axis), and the total velocity magnitude are shown in Figure 16(a)–(f), respectively. From these plots, it is clear that there are considerably more induced vortices for the pFI-3 iteration than the others, and these are caused by the obstacle redirecting the blast wave and thereby reducing its y-component of velocity (Figure 16(c)).

To illustrate this in further detail, the vorticity ($\nabla \times \overrightarrow{v}$), and the kinetic energy, at 4 ms after detonation are plotted in Figure 17(a)–(f), respectively, for each obstacle. It is quite clear from these plots that the interaction of the blast wave with pFI-3 arrangement has significantly influenced the

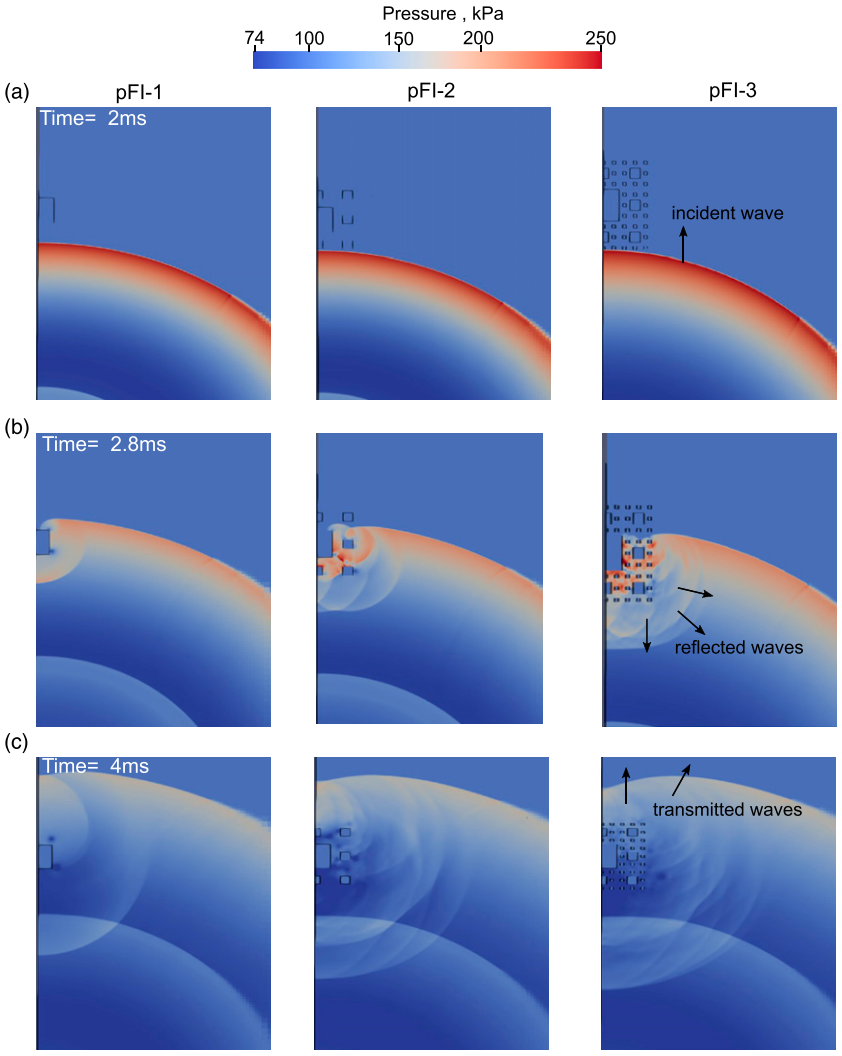

Figure 15. Ground pressure contours at three different time instants arranged row wise: (a) 2 ms, (b) 2.8 ms, and (c) 4 ms for SoD = 2.00 m case. The corresponding obstacles have been arranged column wise: (Left) pFI-1, (Middle) pFI-2, and (Right) pFI-3.

flow field and created more vortices compared to the others, as seen in Figure 17(c). The interaction of diffracted waves with these vortices can significantly influence the flow characteristics (Igra et al., 2013). These vortices serve to transfer energy from the blast wave into lower forms of energy (Needham, 2018), eventually dissipating it as heat, by the lossy viscous action.

The enhanced activity due to the additional vortices in the pFI-3 arrangement directly result in a reduced intensity of kinetic energy in the downstream region, as seen in Figure 17(f) when compared to other arrangements (Figure 17(d) and (e)). Caused by a diversion and dissipation of the kinetic energy, the result is additional downstream mitigation for the pFI-3 arrangement. It has therefore been shown that obstacles with increasingly fractal-like shapes substantially alter the

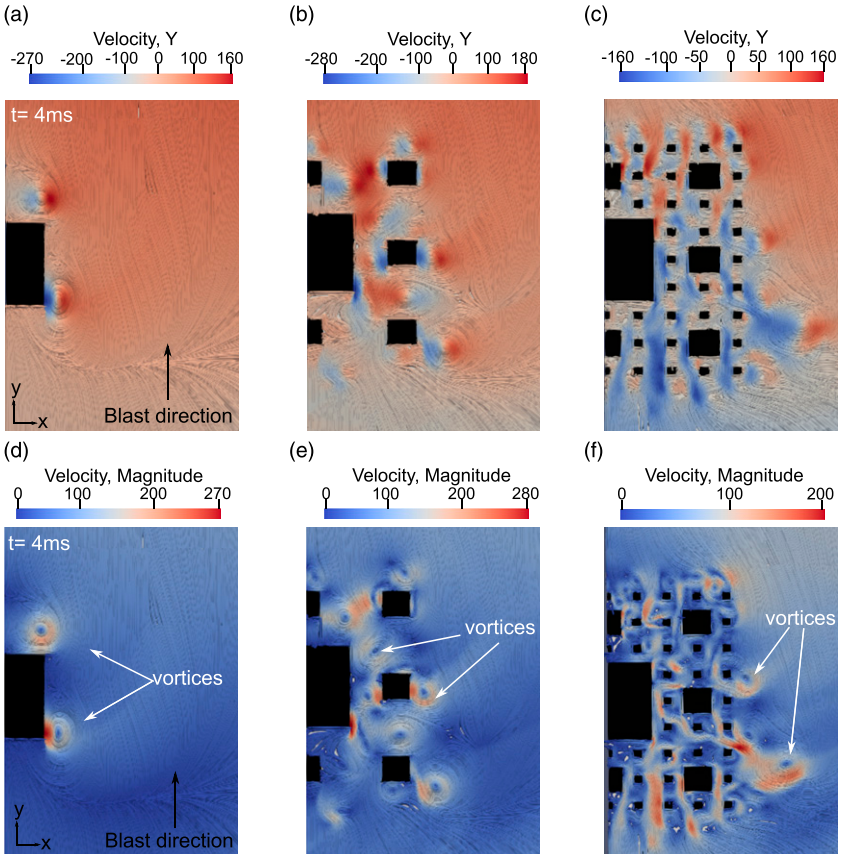

Figure 16. A visualisation of the streamlines at 4 ms coloured in terms of y-velocity magnitude for (a) pFI-1, (b) pFI-2, and (c) pFI-3. The velocity magnitude contours are also given for (d) pFI-1, (e) pFI-2, and (f) pFI-3.

direction of the blast wave from its original path and induce strong vortices, which reduce the kinetic energy and the components of momentum directed downstream (i.e. in the original direction of propagation).

Obstacle impedance

The impedance of each pre-fractal iteration, as defined previously (Figure 13), has been used to quantify and evaluate the role of the pre-fractal complexity in attenuating the strength of the incident blast wave. The reflection and the transmission of the blast wave for all the three blast intensities (SoD125, SoD150, and SoD200) impacting each of the 4 pre-fractal obstacles have been calculated and plotted in Figure 18(a)–(c). At the outset, it is worth mentioning that the mitigation occurs due to changes in the wave reflection and transmission, and due to the formation of vortices. The overall impedance behaviour in Figure 18 is as expected, with increasing complexity of the pre-fractal impeding the blast wave further through enhanced reflection of the incoming wave and a subdued transmission of the incident wave. The inflexion point for both reflection and transmission curves are observed after pre-fractal iteration 2, when the configuration of the obstacles become more

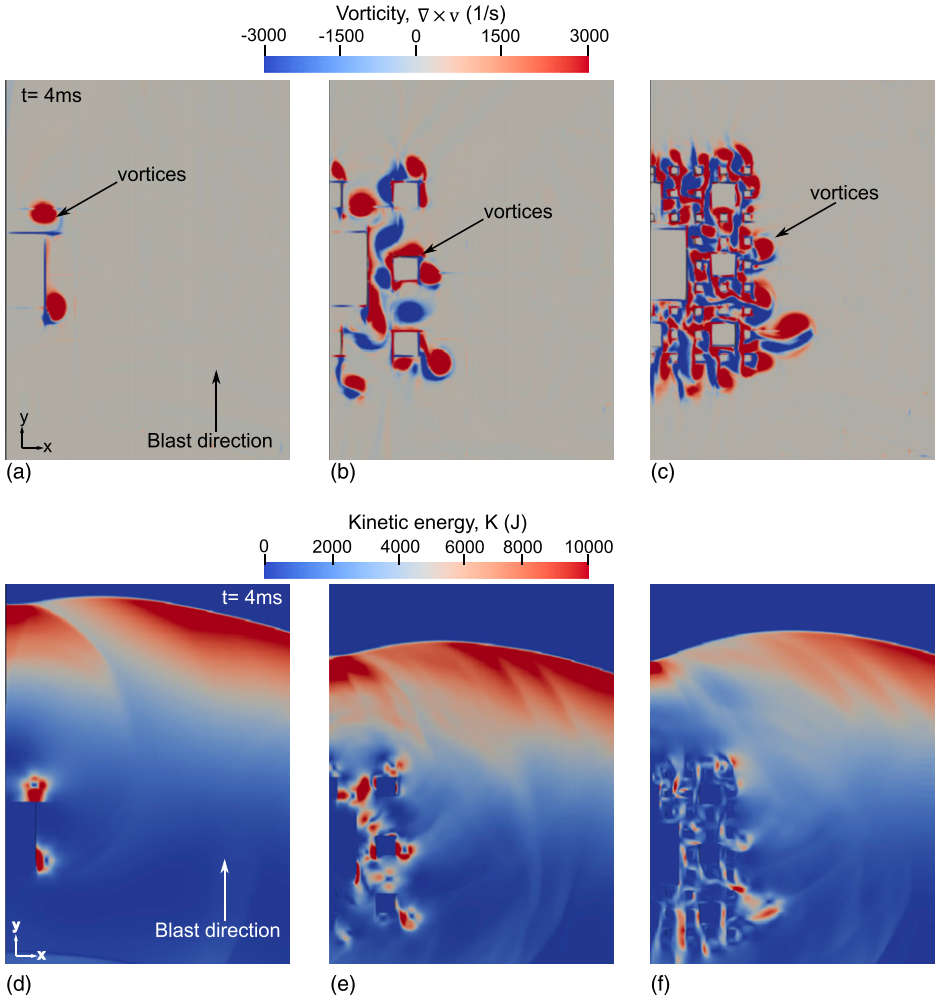

Figure 17. An instantaneous snapshot of the vortices at 4 ms, coloured by magnitude of vorticity for (a) pFI-1, (b) pFI-2, and (c) pFI-3. The contour plots of spatially calculated kinetic energy of the flow field at 4 ms are also given for (d) pFI-1, (e) pFI-2, and (f) pFI-3.

fractal-like. This helps verify yet again that the pFI-3 and pFI-4 configurations would produce higher blast mitigation than pFI-1 and pFI-2.

Ideally, iteration 4 should be the best mitigator since it mostly reflects the pressure wave (and consequently the specific impulse) with the lowest transmitted pressure. However in Figure 18, the specific impulse transmission patterns for pFI-3 and pFI-4 appear to have reached an asymptote as this impedance is at a specific location ($sensor_{out}$ in Figure 13) and so it does not account for the overall behaviour. In the following subsection this aspect of pFI-4 will be highlighted in terms of the blast mitigation in the entire downstream region of the pre-fractal arrangements.

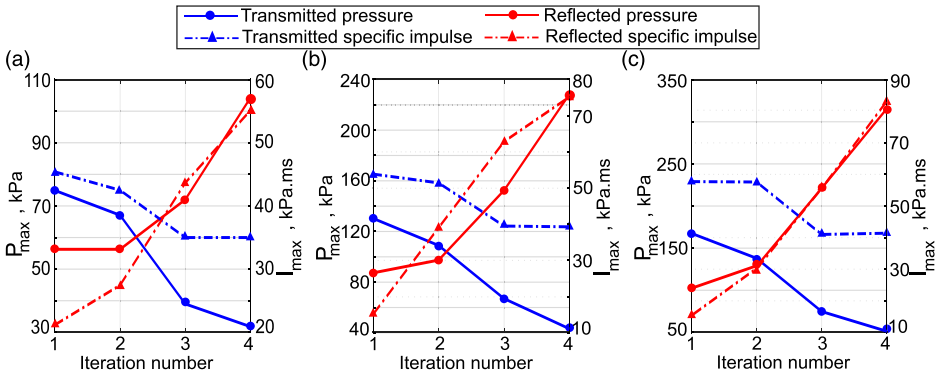

Figure 18. The pre-fractal iteration impedances for three blast wave intensities: (a) SoD = 2.00 m, (b) SoD = 1.50 m, and (c) SoD = 1.25 m.

Spatial bounds of blast mitigation

The mitigation patterns in the downstream are shown as contour plots of pressure and specific impulse (Figures 19 and 20, respectively) for all four pre-fractal arrangements (pFI-1, pFI-2, pFI-3, and pFI-4). These plots also serve to indicate the spatial bounds of the mitigation arising due to the presence of a given obstacle. The spatial coordinates for these plots were normalised using D = 180 mm, the largest length scale in the cross-section of the pre-fractal obstacles.

From Figure 19, it is quite obvious that the pressure reduction behind the obstacle depends on the wave interference at a given location. The mitigation occurs over an increasingly wider zone as the complexity of the pre-fractal shape increases. Their corresponding mitigation values also improve, with up to 60% pressure reduction for pFI-4 (Figure 19(d)). It is worth noting that the more complex obstacle shapes viz., pFI-3 and pFI-4, do not have a strong shock-shock interaction (constructive wave interference) in the downstream (Figure 19(c) and (d)). Such an interaction would have resulted in pressure amplification, as is well documented in literature for 'blocky' obstacles (Alshammari et al., 2022; Hahn et al., 2021; Yang et al., 1987), also observed here for pFI-1 (Figure 19(a)) and pFI-2 (Figure 19(b)).

In addition, the spatial pressure ratios across the length of Y/D at X/D = 0 for pFI-1, pFI-2, pFI-3, and pFI-4 are given in Figure 21, which quantitatively confirms the pressure mitigation effectiveness of pFI-3, and pFI4 and its effect over a greater downstream distance, as well as constructive wave interference of pFI-1 and, in particular, pFI-2. Instead, for these more fractal-like obstacles, a more diffuse and distributed pattern of pressure is obvious. The pressure has been distributed out over a broader region instead of a narrow zone, resulting in improved attenuation as seen in Figure 19(d).

The specific impulse mitigation plots in Figure 20 also show a similar pattern. Even in terms of specific impulse, an increasing complexity of the pre-fractal shape results in an enhanced and widened zone of mitigation. The corresponding specific impulse reduction (Figure 20(d)) reaches up to 40% locally behind the obstacle and remains at around 20% over most of the region that was monitored (10D). This may be attributed to an increase in the frontal area of reflective surfaces, an enhanced wave trapping, and the altered wave interference patterns downstream due to modifications introduced in the directionality of the blast wave.

To probe the temporal evolution of these parameters in the downstream region, two gauges, G1 and G2 (labelled in Figures 19 and 20 and located at X/D =1, Y/D = 3 and X/D = 0, Y/D = 4.5,

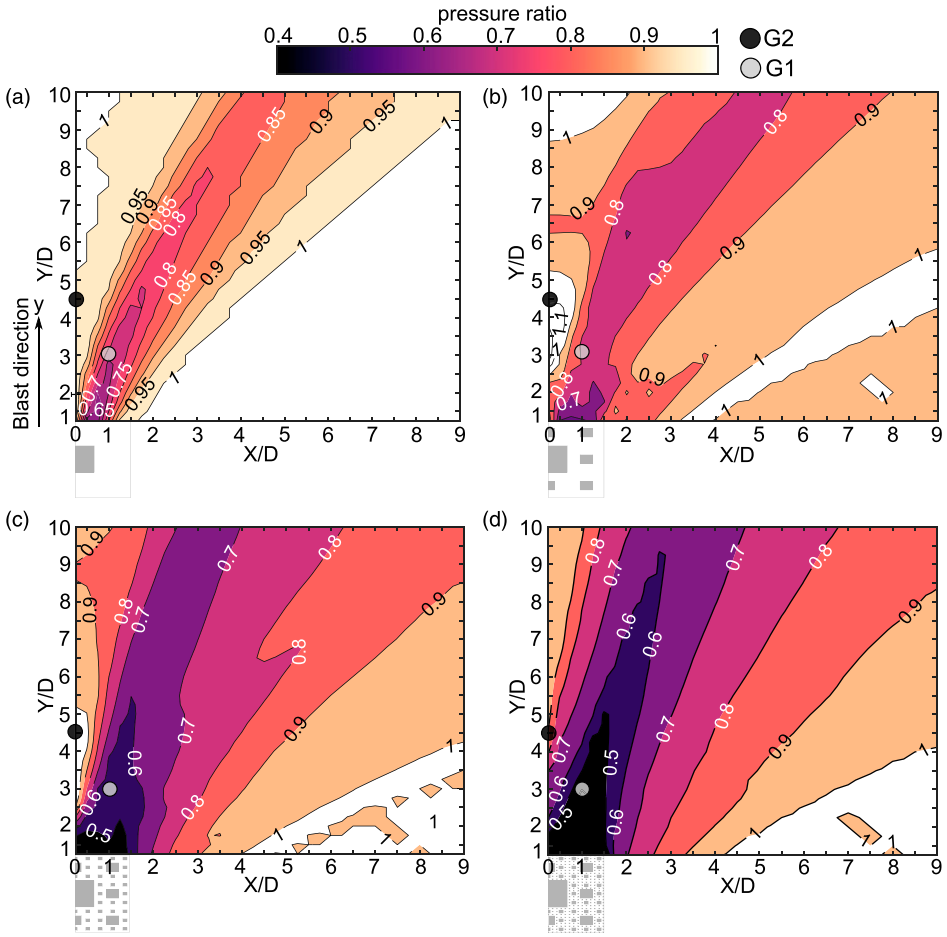

Figure 19. Contour plots of the peak overpressure ratios in the downstream region of the pre-fractal arrangements: (a) pFI-1, (b) pFI-2, (c) pFI-3, and (d) pFI-4.

respectively) were chosen for further investigation. These time history plots, both in terms of the overpressure and the specific impulse, are shown in Figure 22 for all the pre-fractal configurations. With each iteration, there is a delay in the arrival of the shock front at both G1 and G2, and this delay is more pronounced with increasing pre-fractal complexity, supporting the experimental findings of Isaac et al. (2022a). At G1, the reductions in peak overpressure and peak specific impulse correlate with the complexity of the pre-fractal (Figures 22(a) and (b)). From this, it is likely that G1 falls in the destructive interference zone mentioned in Alshammari et al. (2022). However, at G2, while there is a mild increase for the other obstacles, pFI-4 shows a strong attenuation (Figure 22(c)). The peak specific impulse values on the other hand, decreased with increasing complexity of the pre-fractal (Figure 22(d)). These results support the idea that obstacles with a more fractal-like shape can prevent the load amplification caused by constructive wave interference. The effectiveness of obstructing a blast wave, measured in terms of intensity mitigation, may therefore be given as: pFI-4 > pFI-3 > pFI-2 > pFI-1.

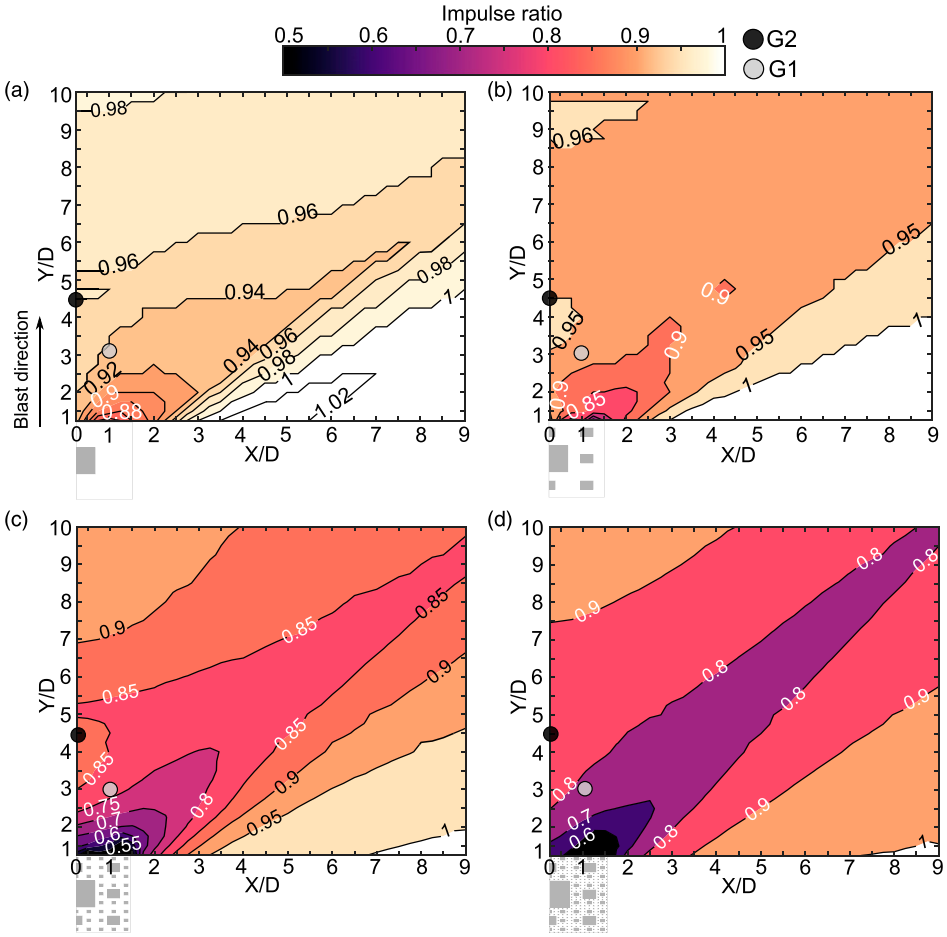

Figure 20. Contour plots of the peak specific impulse ratios in the downstream region of the pre-fractal arrangements: (a) pFI-1, (b) pFI-2, (c) pFI-3, and (d) pFI-4.

Summary and conclusions

Summary

A numerical investigation of blast wave mitigation using pre-fractal shaped obstacles based on the Sierpinski carpet were performed for the experimental configuration of Isaac et al. (2022a) using a physics-based CFD solver, Apollo Blastsimulator. The blast waves in this numerical study were generated using a 0.25 kg hemispherical C4 explosive at three scaled distances $Z = 1.87$, 2.24, and 2.99 m/kg$^{1/3}$. Four pre-fractal obstacle configurations – pFI-1, pFI-2, pFI-3, and pFI-4, and the free-field reference explosion pFI-0 – were modelled after the experimental setup.

The fidelity of this CFD solver in recreating complex blast wave-obstacle interactions was demonstrated using a detailed, multi-part mesh sensitivity analysis that involved both quantitative and qualitative comparison with experimental data. This comparison included validating pressure histories at select locations in the flow domain, and a qualitative comparison of the numerical shock

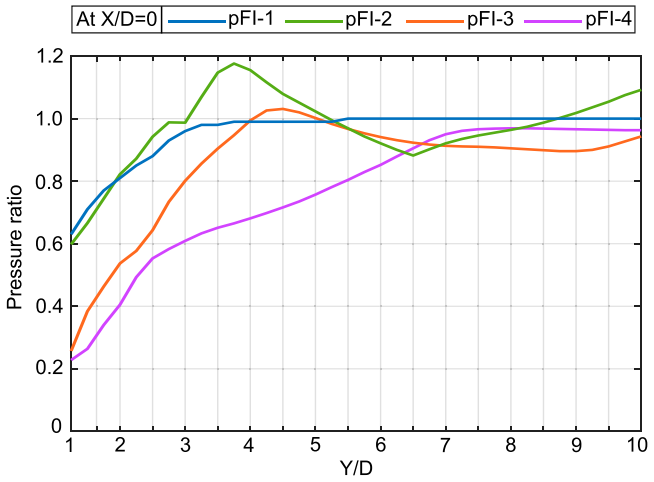

Figure 21. Spatial pressure ratios of pFI-1, pFI-2, pFI-3, pFI-4 extracted from Figure 19 for the length of Y/D at X/D = 0.

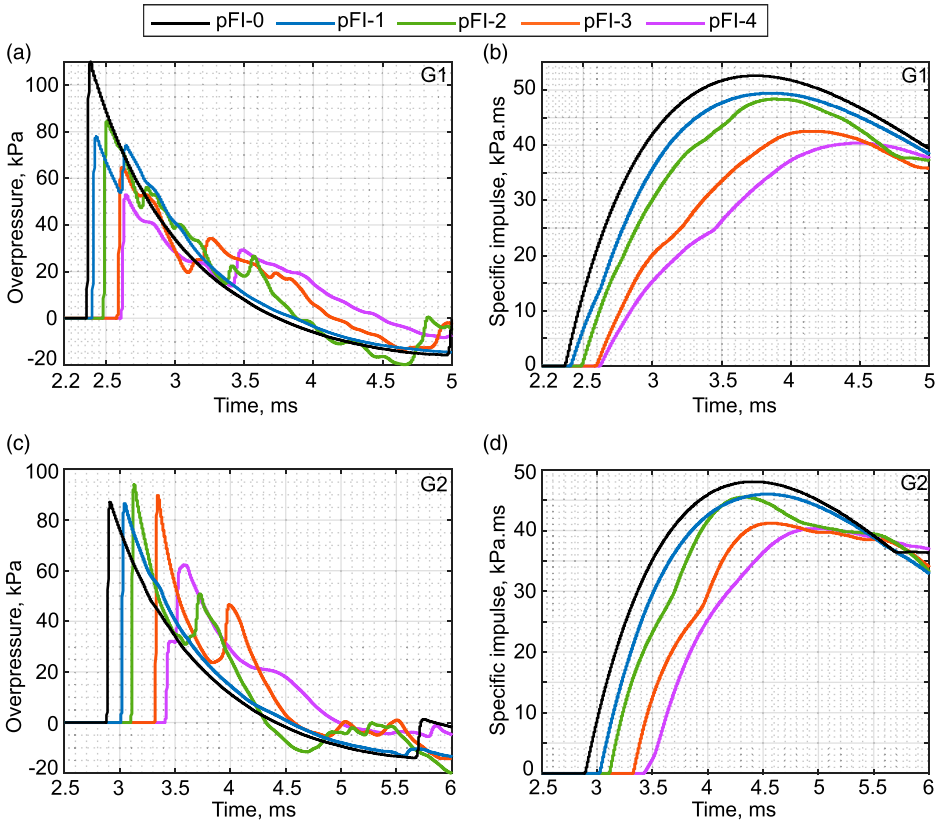

Figure 22. Overpressure and specific impulse histories at (a),(b) G1 and (c),(d) G2 for all pre-fractal obstacles: pFI-1, pFI-2, pFI-3, and pFI-4 and the reference pFI-0.

front with time-resolved flow field images. It was found that a mesh size (defined using the ratio of the smallest obstacle's width to the minimum mesh element size) greater than 2 was sufficient to reliably capture the reflection patterns, the wave entrapment, and the changes to the flow direction due to the presence of the obstacle.

The primary aim of this numerical work was to understand the mechanics of the enhanced blast mitigation reported experimentally for pre-fractal-like shapes such as pFI-3. Subsequently, the effectiveness of increasing the complexity of the pre-fractals by another iteration (pFI-4) was studied. Finally, the relationship between the pre-fractal configuration and the spatial bounds of the ensuing blast mitigation were explored.

Conclusions

Enhanced blast mitigation in the downstream region was observed for obstacles that more closely resemble a true fractal (such as pFI-3). This was found to be due to the strength of the wave reflection and the intensification of trapping within the confines of the fractal, which resulted in a reduction in the proportion of incident pressure transmitted downstream. Findings were related to the concept of impedance, and increasing pre-fractal iterations were shown exhibit higher impedance (i.e. enhanced wave reflection and reduced wave transmission).

Additionally, fractal-like shapes were found to significantly alter the direction of the incident wave and generate additional vorticity that led to a further reduction of kinetic energy and momentum in the direction of the blast wave. The role of increasing the pre-fractal by another iteration (pFI-4) was numerically assessed and it was confirmed that this higher complexity pre-fractal could further enhance reflection and diminish the transmission of the incident wave.

The mitigation of pressure and specific impulse in the downstream region occurred along zones associated with the location of destructive wave interference patterns in the downstream region. Such zones were found to widen spatially as the complexity of the pre-fractal increased, leading to improved mitigation. Strong shock-shock interactions that result in load amplification, commonly encountered in downstream regions of a solitary block-like obstacle, were not observed for the more fractal-like shapes, for example, pFI-3 and pFI-4. Specifically, the peak reduction in pressure and specific impulse in the downstream region of the pFI-4 pre-fractal arrangement were found to be 60% and 40%, respectively. It was thus concluded that complex pre-fractal obstacles can more effectively mitigate an explosion in the mid-field (pFI-4 > pFI-3 > pFI-2 > pFI-1).

The findings in this work are significant in that they confirm the complex behaviour driving mitigation through blast interaction with complex obstacles. Further, rigorous validation of numerical modelling and clear guidance on requirements in terms of model fidelity facilitate further research and design in this area.

Declaration of conflicting interests

The author(s) declared no potential conflicts of interest with respect to the research, authorship, and/or publication of this article.

Funding

The author(s) disclosed receipt of the following financial support for the research, authorship, and/or publication of this article: This work was supported by the University of Hail (40/4/23077) and Engineering and Physical Sciences Research Council (EP/S037241/1).

ORCID iDs

Omar Ghareeb Alshammari https://orcid.org/0000-0003-3419-8054
Obed Samuelraj Isaac https://orcid.org/0000-0003-3621-5903
Samuel Edward Rigby https://orcid.org/0000-0001-6844-3797

Notes

1. A fractal is mathematical concept of an object that has a self-repeating pattern embedded within itself, i.e. it is multi-scale and self-similar by definition. Whilst a true fractal comprises an infinite number of repetitions (or iterations) of the pattern, practically a truncated version of this concept, involving a finite number of iterations, is required. A finite-iteration fractal is termed a 'pre-fractal'.
2. Note that domain length labels refer to the three different stand-off distances ultimately studied, however, in this mesh sensitivity study, only the smallest domain and shortest stand-off distance was required.
3. The case of pFI-3 with SoD125 in Figure 10(c) is a repeat of Figure 6(c).
4. Ideally, it should have been a square rod of side = $1/3^{rd}$ of 20 mm (since S=3 for this fractal) with an identical 6.33 mm gap, but due to certain constraints in mesh generation, 7.5 mm has been used herein.
5. i.e., an impedance of zero would result in zero reflection and full transmission of the wave, an infinite impedance would result in full reflection and zero transmission, therefore an increase in reflection and decrease in transmission signifies an increase in apparent impedance.

References

Alshammari OG, Isaac OS, Clarke SD, et al. (2022) Mitigation of blast loading through blast–obstacle interaction. *International Journal of Protective Structures* 204141962211158.

Beyer ME (1986) *Blast Loads behind Vertical Walls*. California: Prepared for Twenty-Second DoD Explosives Safety Seminar Anaheim.

Bogosian D, Yokota M and Rigby S (2016) TNT equivalence of C-4 and PE4: a review of traditional sources and recent data. In: Proceedings of the 24th military aspects of blast and shock, Halifax, Nova Scotia, Canada, September 2016.

Chaudhuri A, Hadjadj A, Sadot O, et al. (2013) Numerical study of shock-wave mitigation through matrices of solid obstacles. *Shock Waves* 23: 91–101.

Christiansen AP and Bogosian DD (2012) Limitations and consequences of fragment protection for near-field airblast measurements. In: 83rd Shock & Vibration Symposium, New Orleans, 4–8 November, *Paper U-086*. pp. 1–10.

Dadrasi A, Beynaghi M and Fooladpanjeh S (2019) Crashworthiness of thin-walled square steel columns reinforced based on fractal geometries. *Transactions of the Indian Institute of Metals* 72(1): 215–225.

Dattelbaum DM, Ionita A, Patterson BM, et al. (2020) Shockwave dissipation by interface-dominated porous structures. *AIP Advances* 10(7): 075016.

Dennis AA, Pannell JJ, Smyl DJ, et al. (2021) Prediction of blast loading in an internal environment using artificial neural networks. *International Journal of Protective Structures* 12(3): 287–314.

Farrimond DG, Woolford S, Tyas A, et al. (2023) Far-field positive phase blast parameter characterisation of RDX and PETN based explosives. *International Journal of Protective Structures* 204141962211497.

Fraunhofer EMI (2018) Apollo blastsimulator manual, version: 2018.2. Freiburg, Germany: Fraunhofer Institute for High-Speed Dynamics, Ernst-Mach-Institut.

Gautier A, Sochet I, Lapebie E, et al. (2020) Shock wave propagation in an obstructed area. *WIT Transactions on The Built Environment* 198: 15–27.

Gebbeken N and Döge T (2010) Explosion protection—architectural design, urban planning and landscape planning. *International Journal of Protective Structures* 1(1): 1–21.

Gebbeken N, Warnstedt P and Rüdiger L (2017) Blast protection in urban areas using protective plants. *International Journal of Protective Structures* 9(2): 226–247. DOI:10.1177/2041419617746007.

Hahn A, Mensinger M and Rutner M (2021) Peak overpressure and impulse due to diffraction over a cylinder and/or multi-reflection of a shock wave in structural design-Part I. *International Journal of Protective Structures* 12(1): 22–48.

Hao Y, Hao H, Shi Y, et al. (2017) Field testing of fence type blast wall for blast load mitigation. *International Journal of Structural Stability and Dynamics* 17(09): 1750099.

Higham J and Brevis W (2018) Modification of the modal characteristics of a square cylinder wake obstructed by a multi-scale array of obstacles. *Experimental Thermal and Fluid Science* 90: 212–219.

Higham J and Vaidheeswaran A (2022) Modification of modal characteristics in the wakes of blockages of square cylinders with multi-scale porosity. *Physics of Fluids* 34(2): 025114.

Higham J, Vaidheeswaran A, Brevis W, et al. (2021) Modification of modal characteristics in wakes of square cylinders with multi-scale porosity. *Physics of Fluids* 33(4): 045117.

Igra O, Falcovitz J, Houas L, et al. (2013) Review of methods to attenuate shock/blast waves. *Progress in Aerospace Sciences* 58: 1–35.

Isaac OS, Alshammari OG, Clarke SD, et al. (2022a) Experimental investigation of blast mitigation of pre-fractal obstacles. *International Journal of Protective Structures* 204141962211440.

Isaac OS, Alshammari OG, Pickering EG, et al. (2022b) Blast wave interaction with structures–An overview. *International Journal of Protective Structures* 204141962211185.

Jin M, Hao Y and Hao H (2019) Numerical study of fence type blast walls for blast load mitigation. *International Journal of Impact Engineering* 131: 238–255. DOI:10.1016/j.ijimpeng.2019.05.007.

Klomfass A (2018) Accuracy of cfd predictions for explosive far fields. In: 25th International Conference on Military Aspects of Blast and Shock (MABS252), The Hague, Netherlands.

Meza LR, Zelhofer AJ, Clarke N, et al. (2015) Resilient 3D hierarchical architected metamaterials. *Proceedings of the National Academy of Sciences* 112(37): 11502–11507.

Needham C (2018) *Blast Waves*. Cham: Springer International Publishing.

Nguyen-Van V, Wu C, Vogel F, et al. (2021) Mechanical performance of fractal-like cementitious lightweight cellular structures: numerical investigations. *Composite Structures* 269: 114050.

Niollet J, Yuen SCK and Nurick G (2015) A study to assess the use of cylindrical bars as blast barriers. *International Journal of Protective Structures* 6(2): 263–286.

Pannell J, Rigby S, Panoutsos G, et al. (2019) Predicting near-field specific impulse distributions using machine learning. In: 18th International Symposium on Interaction of the Effects of Munitions with Structures (ISIEMS18), Panama City Beach, FL, USA.

Pannell JJ, Panoutsos G, Cooke SB, et al. (2021) Predicting specific impulse distributions for spherical explosives in the extreme near-field using a Gaussian function. *International Journal of Protective Structures* 12(4): 437–459.

Prasanna Kumar SS, Patnaik BSV and Ramamurthi K (2018) Prediction of air blast mitigation in an array of rigid obstacles using smoothed particle hydrodynamics. *Physics of Fluids* 30(4): 046105. DOI:10.1063/1.5022198.

Rigby SE and Sielicki PW (2015) An investigation of TNT equivalence of hemispherical PE4 charges. *Engineering Transactions* 62(4): 423–435.

Skews BW, Draxl MA, Felthun L, et al. (1998) Shock wave trapping. *Shock Waves* 8(1): 23–28.

Sreenivasan K (1991) Fractals and multifractals in fluid turbulence. *Annual Review of Fluid Mechanics* 23(1): 539–604.

Suzuki K, Himeki H, Watanuki T, et al. (2000) Experimental studies on characteristics of shock wave propagation through cylinder array. *The Institute of Space and Astronautical Science* 676.

Turcotte DL (1988) Fractals in fluid mechanics. *Annual Review of Fluid Mechanics* 20(1): 5–16.

Werner DH and Ganguly S (2003) An overview of fractal antenna engineering research. *IEEE Antennas and Propagation Magazine* 45(1): 38–57.

Whittaker M, Klomfass A, Softley I, et al. (2019) Comparison of numerical analysis with output from precision diagnostics during near-field blast evaluation. In: *18th International Symposium on Interaction of the Effects of Munitions with Structures (ISIEMS18)*, Panama City Beach, FL, 21–25 October 2019.

Xiao W, Andrae M and Gebbeken N (2017) Numerical prediction of the shock wave mitigation effect using protective barriers made of steel posts with a square hollow section. In: 17th International Symposium on the Interaction of the Effects of Munitions with Structures (ISIEMS). Bad Neuenahr, Germany, 16–20 October.

Xiao W, Andrae M and Gebbeken N (2020) Numerical study on impulse reduction performance of protective barriers made of steel posts. *Journal of Structural Engineering* 146(10): 04020197.

Yang J, Liu Y and Lomax H (1987) Computation of shock wave reflection by circular cylinders. *AIAA Journal* 25(5): 683–689.

Zong R, Hao H and Shi Y (2017) Development of a new fence type blast wall for blast protection: numerical analysis. *International Journal of Structural Stability and Dynamics* 17(06): 1750066.